Boosting Alkaline Nitrate Reduction to Ammonia via Molybdenum-Mediated Hydrogenation on CuO Nanoarrays

*Yanwei Wang,[a] Zhexuan Li, [b] Jisong Hu [c] and Ling Fang *[b]*

a. Xuzhou College of Industrial Technology, Xuzhou, 221140, China
b. Chongqing Institute of Green and Intelligent Technology, Chinese Academy of Sciences, Chongqing 400714, China
c. Advanced Materials and Devices Laboratory, School of Materials Science and Engineering, School of Chemistry and Environmental Engineering, Hanshan Normal University, Chaozhou, 521041, China

Preparation of Mo-doped CuO NAs

A piece of copper foam (4.0 × 2.0 cm^2) was immersed in 3 M HCl and cleaned in an ultrasonic bath for 5 min. The foam was then rinsed with deionized water (DIW). Subsequently, the copper foam was immersed in anhydrous ethanol, cleaned in an ultrasonic bath for 3 min, and transferred to a vacuum drying oven at 30 °C for 90 min.

A solution was prepared by adding 16 g of NaOH and 3.2 g of ammonium persulfate to 70 mL of DIW, and stirring until homogeneous. The dried copper foam was placed into this solution and heated in a water bath with stirring (60 °C, 20 min, 160 rpm). After oscillation, the resulting CuO NAs were obtained, rinsed with DIW, cleaned in an ultrasonic bath with anhydrous ethanol for 3 min, and finally dried in a vacuum oven at 60 °C for 240 min.

To synthesize Mo-doped CuO, various concentrations of ammonium heptamolybdate tetrahydrate ($(NH_4)_6Mo_7O_{24}\cdot 4H_2O$, 1 mM, 2 mM, 4 mM) were dissolved in 30 mL of DIW. The solution was stirred until homogeneous and transferred into a 50 mL stainless steel autoclave with a polytetrafluoroethylene (PTFE) lining. CuO NAs were placed into the autoclave, which was then sealed and maintained at 140 °C for 6 h. The obtained samples were washed several times with water and ethanol, then dried in a vacuum oven at 60 °C for 12 h. The resulting products were labeled as Mo_1-CuO, Mo_2-CuO, and Mo_4-CuO according to the Mo concentration.

Characterizations

The surface morphologies of the catalysts were recorded by field-emission scanning electron microscope (SEM, JSM-7800F), transmission electron microscopy (TEM, Talos F200S). The composition and crystalline structure were characterized by X-ray diffraction (XRD, X'Pert3 Powder), X-ray photoelectron spectrometery (XPS) with a ESCALAB250 analyzer.

Raman measurement was performed on RENISHAW inVia Raman Microscope. The *in situ* Raman measurement was carried out by the aforementioned Raman microscope and electrochemical workstation. The electrolytic cell was homemade by Teflon with a quartz window between the sample and objective. The working electrode was immersed into the electrolyte through the wall of the cell and kept the electrode plane perpendicular to the laser. A platinum wire and Ag/AgCl were used as the counter and reference electrode, respectively. A 532 nm laser with 50 mW was used as an excitation source and the laser was focused on the catalyst surface using a 50× objective. The spectra were acquired from a single spot on the electrode, taken as a laser power and expose time of 5% and 30 s, respectively.

Electrochemical Measurements

Electrochemical experiments were carried out in a two-compartment H-type cell with magnetic stirring at 400 rpm, using a Shanghai Chenhua CHI660E and a Parstat 2273 electrochemical workstation. A three-electrode configuration was employed: Mo_1-CuO, Mo_2-CuO, and Mo_4-CuO as working electrodes (1.0 × 1.0 cm^2), a Hg/HgO electrode (filled with 1 M KOH solution) as the reference electrode, and a Ru-Ir-Ti electrode as the counter electrode. Prior to testing, the cathode compartment was filled with 100 mL of electrolyte containing 0.5 M KOH and 100 mg L^{-1} KNO_3.

Cyclic voltammetry (CV) was conducted in the potential range from 0.4 V to -0.6 V vs. RHE at a scan rate of 50 mV s^{-1}. Linear sweep voltammetry (LSV) curves were recorded at room temperature from 0.4 V to -0.6 V vs. RHE at a scan rate of 10 mV s^{-1}. In addition, to determine the electrochemical double-layer capacitance (C_{dl}), CV tests were performed in a non-Faradaic potential region at different scan rates of 10, 15, 20, 25, 30, and 40 mV s^{-1}. Electrochemical impedance spectroscopy (EIS) measurements were performed in the frequency range from 100 kHz to 0.1 Hz at the open-circuit and reaction potentials, with an amplitude perturbation of 5 mV.

Detection of Ammonia, Nitrite, and Nitrate

Nitrate-N Analysis:

1.0 mL of electrolyte was extracted and diluted to a volume suitable for detection. Next, 1 mL of 1 M HCl and 0.1 mL of 0.8 wt% sulfamic acid solution were added to the diluted electrolyte. Absorption readings at 220 nm and 275 nm were taken using a UV-Vis spectrophotometer. The final absorption intensity was calculated as A = A220nm - A275nm. A calibration curve for concentration versus absorbance was created using a series of standard potassium nitrate solutions, with potassium nitrate powder pre-dried at 105-110 °C for 2 hours.

Nitrite-N Analysis:

1.0 mL of electrolyte was taken and diluted to the appropriate detection range. A color reagent mixture, consisting of ultrapure water (500 mL), phosphoric acid (50 mL, 15 M), 4-aminobenzenesulfonamide (20.0 g), and N-(1-naphthyl)ethylenediamine dihydrochloride (1.00 g), was prepared. After adding a measured amount of this reagent to the diluted electrolyte, the solution was allowed to react for 20 minutes. The absorption intensity at 540 nm was then measured using a UV-Vis spectrophotometer. A calibration curve was established using standard sodium nitrite solutions.

Ammonia-N Analysis:

1.0 mL of electrolyte was extracted and diluted to a suitable detection range. Potassium sodium tartrate solution (ρ = 500 g/L) was mixed into the diluted electrolyte, followed by the addition of Nessler's reagent. After allowing the solution to react for 10 minutes, the absorption intensity at 420 nm was recorded using a UV-Vis spectrophotometer. The concentration-absorbance curve was calibrated using standard ammonium chloride solutions, with ammonium chloride powder pre-dried at 105 °C for 2 hours.

Computational methods

All density functional theory (DFT) computations in this study were conducted with the Vienna Ab initio Simulation Package (VASP). The exchange-correlation energy was treated by Perdew-Burke-Ernzerhof (PBE) functional within the generalized gradient approximation (GGA), and the ion-electron interactions were described by the projector augmented-wave method. The electronic convergence criterion was set to a total energy difference of 10^{-5} eV between successive self-consistent field steps. A geometry optimization was considered convergent when the force change was smaller than 0.03 eV/Å. A 2 × 3 × 1 Monkhorst-Pack k-point grid was adopted for Brillouin

zone sampling, and all calculations were performed with spin polarization effect. To clarify the basis for surface model selection, both CuO(111) and CuO(110) slabs were initially constructed and the adsorption free energies of NO_3^- on the two surfaces were compared. The adsorption free energy of NO_3^- on CuO(110) is 2.17 eV lower than that on CuO(111) (−0.95 eV versus 1.22 eV), indicating that nitrate adsorption is thermodynamically more favorable on CuO(110). Therefore, the CuO(110) surface was employed for the subsequent adsorption and reaction free-energy calculations. A vacuum layer of 15Å was employed to avoid interactions of neighboring images. The ΔG of NO_3RR steps were calculated by: $\Delta G = \Delta E_{DFT} + \Delta E_{ZPE} - T\Delta S$, where ΔE_{DFT}, ΔE_{ZPE}, and ΔS are the energy from DFT optimization, correction of zero-point energy, and the variation of entropy, respectively.

Table S1. Comparison of the NO_3^- to NH_3 electrocatalytic performance of this work with recently reported Cu- and Mo-based electrocatalysts.

Catalysts	Electrolyte	NH_3 yield rate	FE_{NH_3}	Ref.
Fe-MoS_2/CC	0.1 M KOH	12.5μg h^{-1} cm^{-2}	10.8	1
Cu-Pd/C NBs	0.1 M KOH	220.8 μg h^{-1} mg_{cat}^{-1}	62.3	2
Ru-Cu NW	1 M KOH	76.5 mg h^{-1} cm^{-2}	90	3
Cu-N-C SAC	1 M KOH	212.5 mg $g^{-1}{}_{Cu}$ h^{-1}	84.7	4
B-MoS_2/CC	0.5 M $NaSO_4$	10.8 mg h^{-1} cm^{-2}	92.3	5
Cu/CuAu ordered SAA	1 M KOH	8.47 mol h^{-1} g^{-1}	85.5	6
Fe/Cu-HNG	1 M KOH	1.08 mmol h^{-1} g^{-1}	60	7
o-CoP/C@Cu_3P/CF^s	1 M KOH	1.571 mmol h^{-1} g^{-1}	90.27	8
RuMo	0.1 M KOH	32.7 mg h^{-1} mg_{cat}^{-1}	95.2	9
FeCo-$Mo_{0.82}$N/NC	0.1 M K_2SO_4	12.28 mg h^{-1} mg_{cat}^{-1}	83.24	10
This work	0.5 M KOH	7.8 ± 0.1 mg h^{-1} cm^{-2}	90.1	

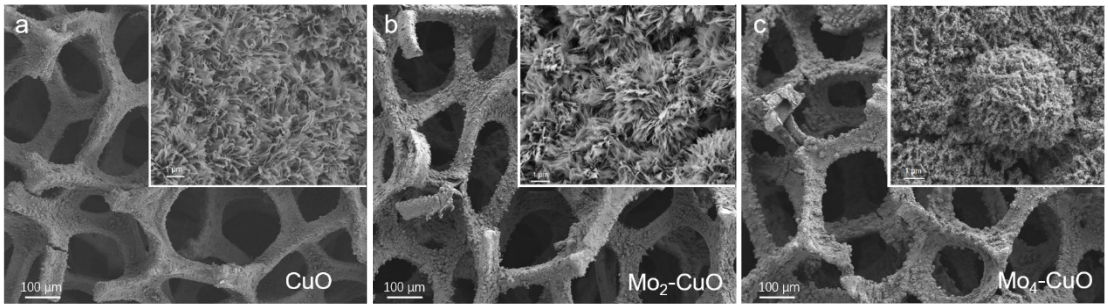

Fig. S1 SEM images of (a) CuO, (b) Mo_2-CuO, and (c) Mo_4-CuO.

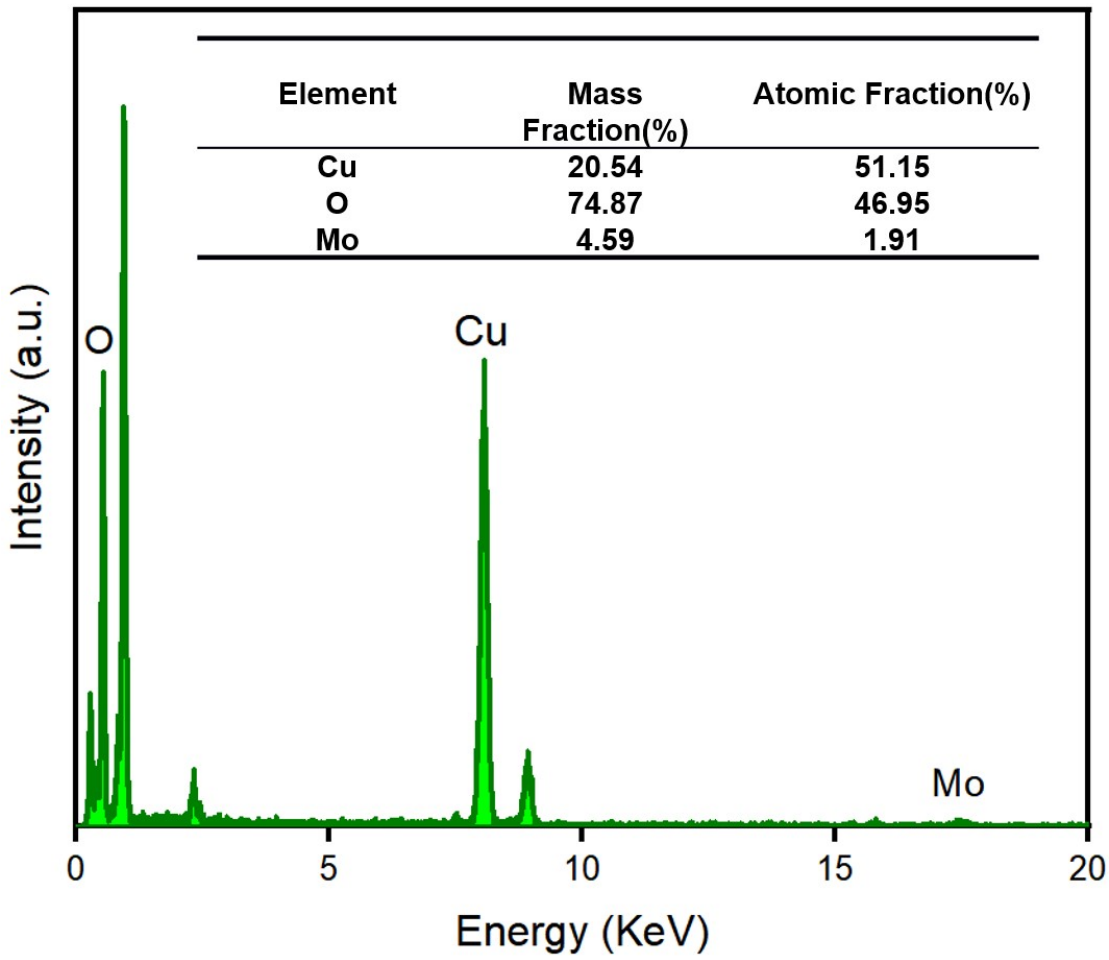

Fig. S2 EDX elemental contents of Mo_1-CuO.

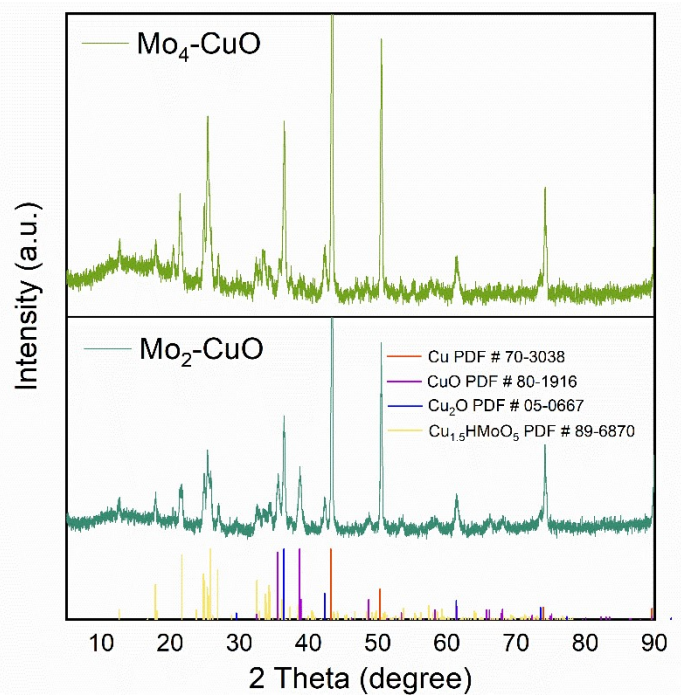

Fig. S3 XRD profile of Mo_2-CuO and Mo_4-CuO catalysts.

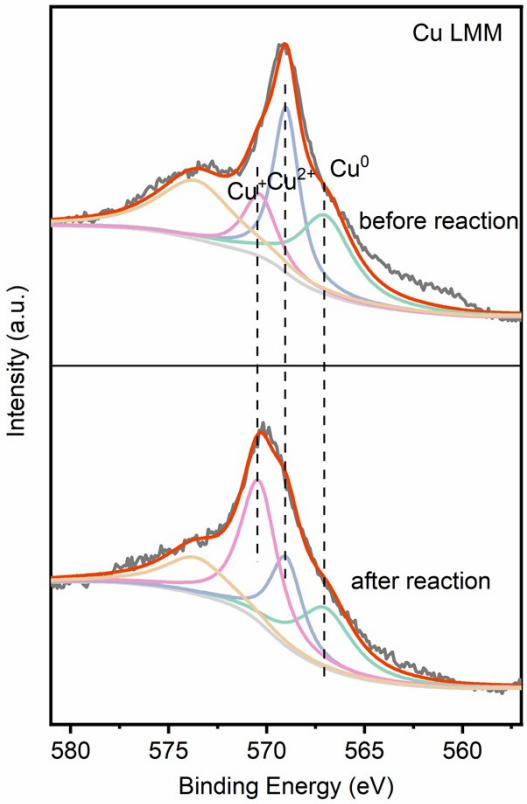

Fig. S4 Cu LMM Auger electron spectra of Mo_1-CuO before and after the NO_3RR electrolysis.

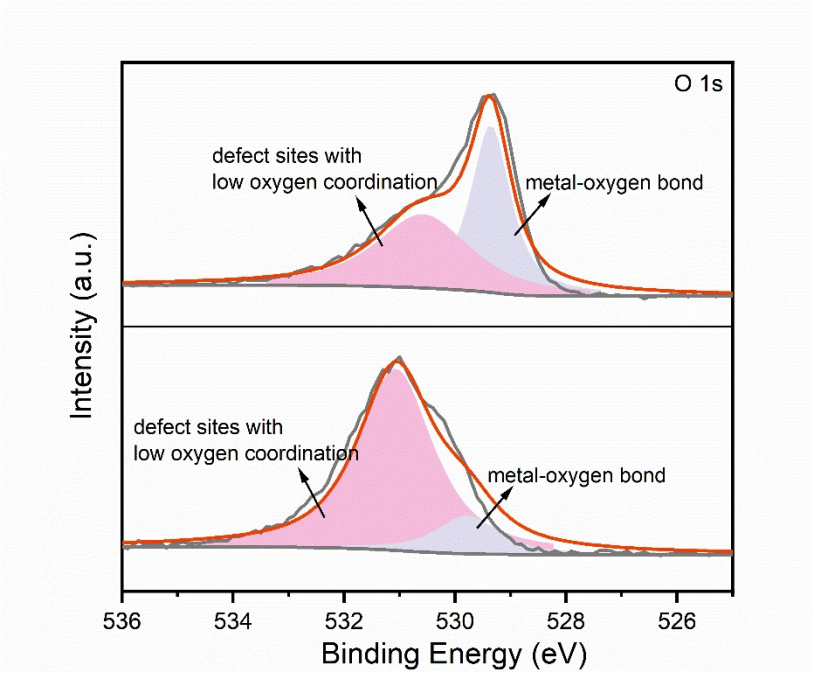

Fig. S5 XPS of O 1s before and after NO_3RR

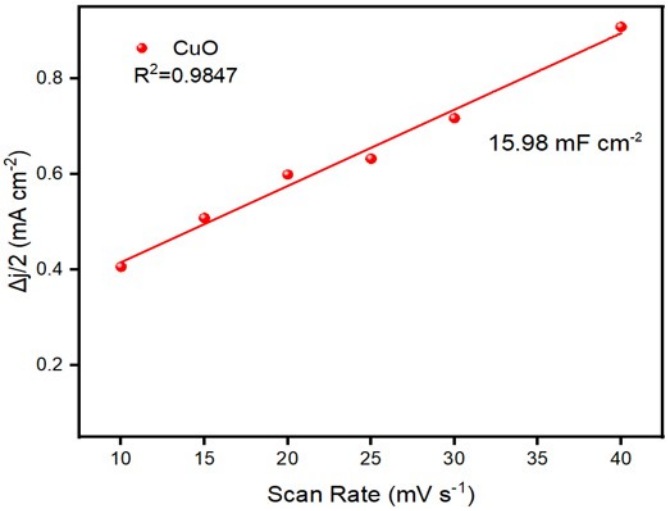

Fig. S6 Relationship between current density and scan rate for CuO.

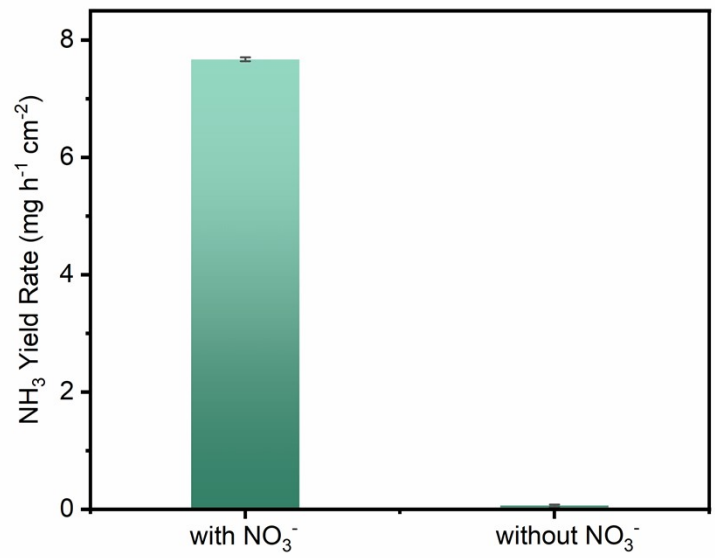

Fig. S7 The NH_3 yield rate on Mo_1-CuO catalyst with and without NO_3^-.

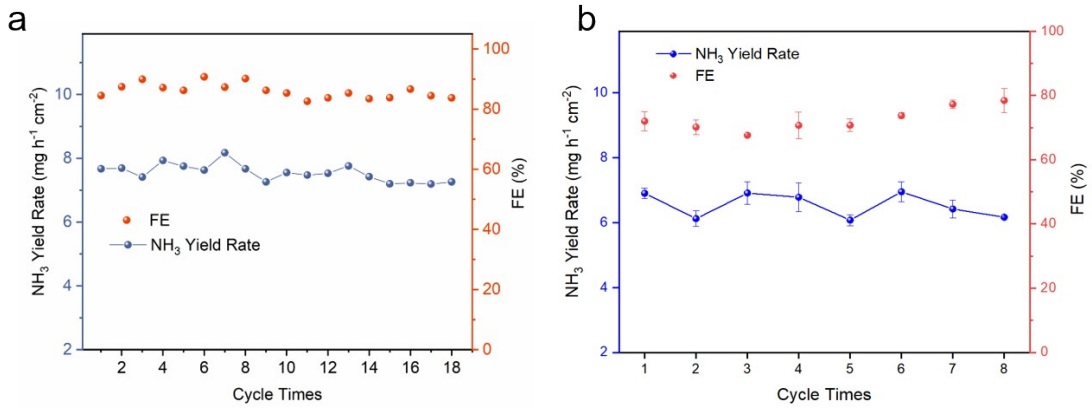

Fig. S8 Cycling stability test of (a) Mo_1-CuO and (b) CuO.

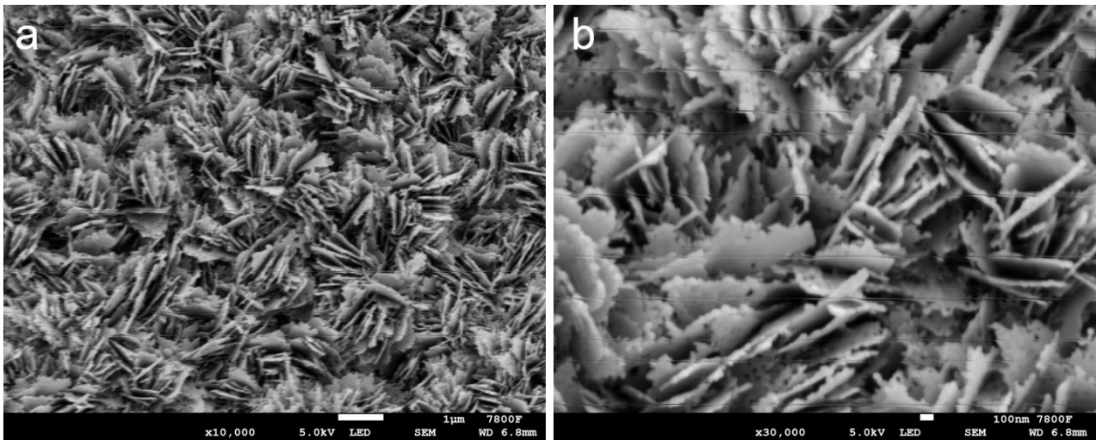

Fig. S9 (a-b) SEM images of Mo_1-CuO after NO_3RR at different magnifications.

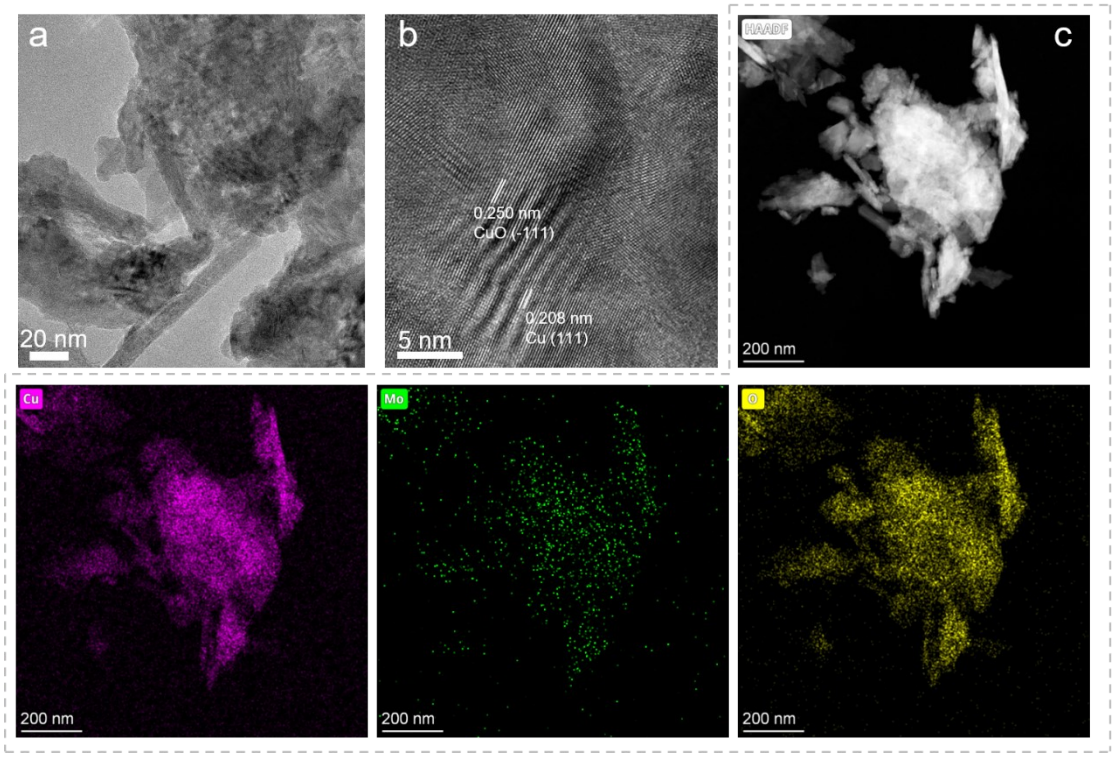

Fig. S10 (a-b) TEM images and (c) EDX elemental mapping images of Mo_1-CuO after NO_3RR.

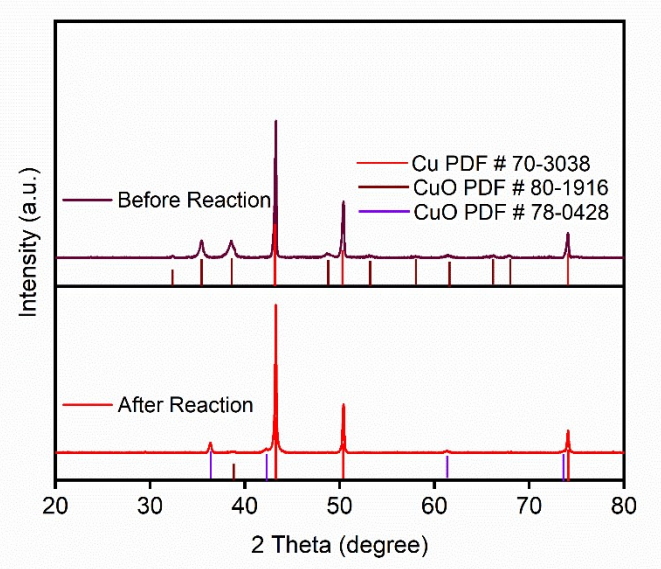

Fig. S11 XRD spectra of Mo_1-CuO before and after NO_3RR.

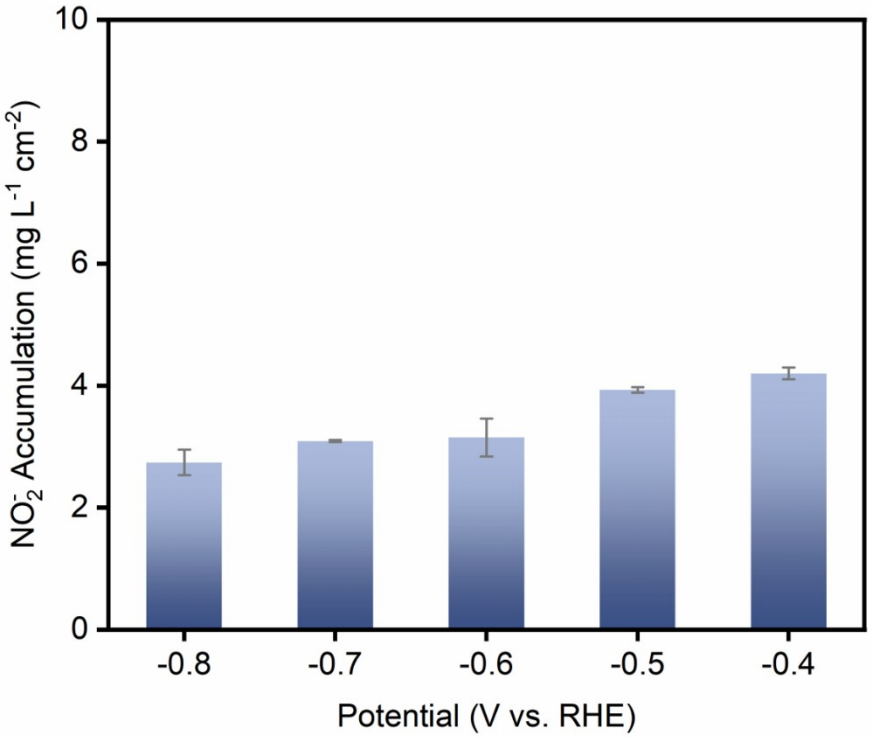

Fig. S12 The NO_2^- accumulation at different potentials for Mo_1-CuO.

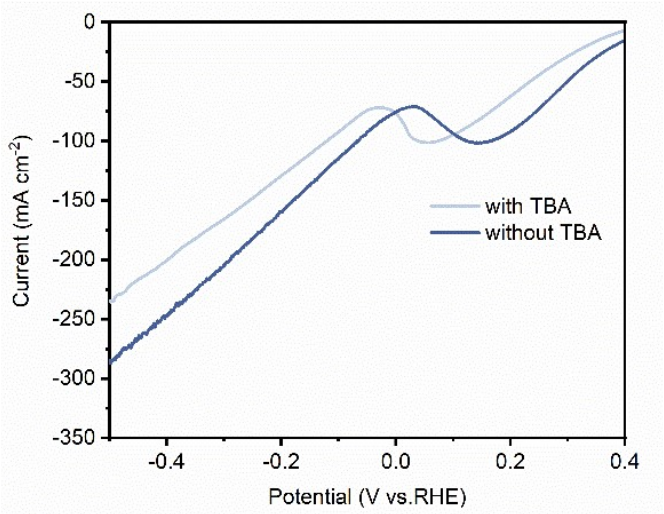

Fig. S13 The LSV curves of Mo_1-CuO with and without TBA.

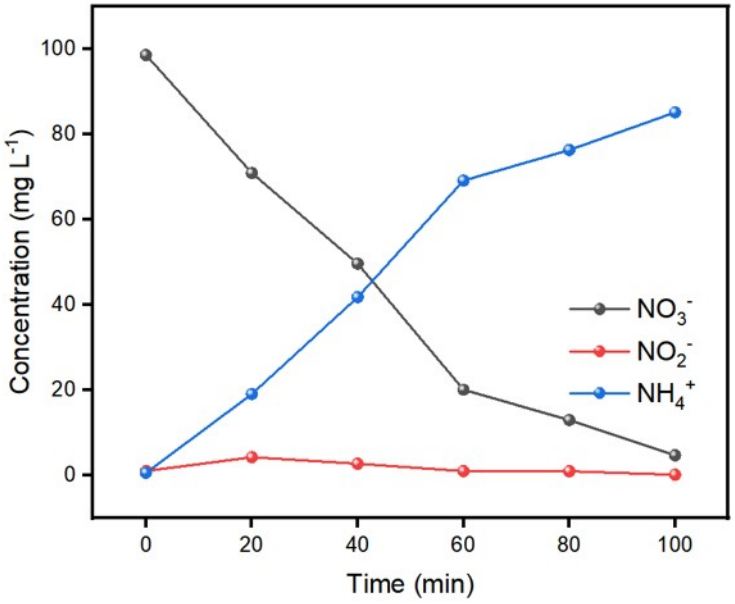

Fig. S14 Changes in reactants and products over time under Mo_1-CuO catalysis.

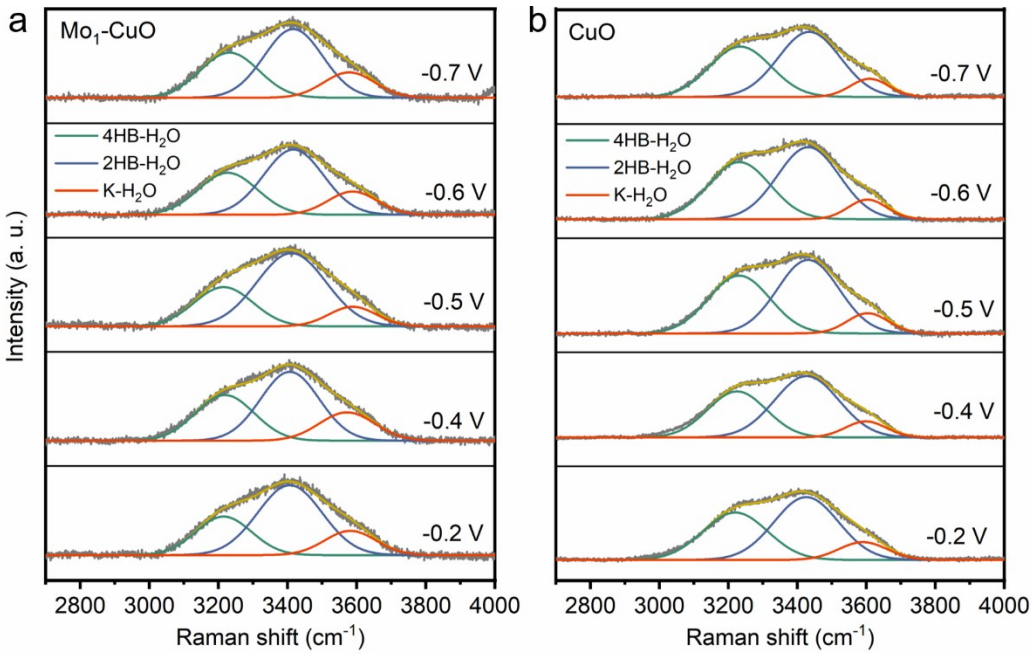

Fig. S15 Potential-dependent in situ Raman spectra of the O-H stretching mode of interfacial water on (a) Mo_1-CuO and (b) CuO.

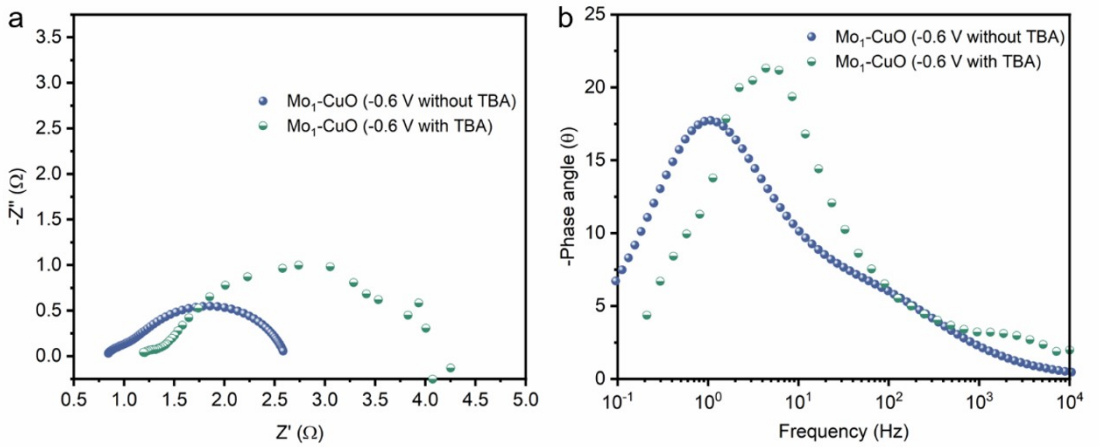

Fig. S16 (a) Nyquist plot and (b) Bode plot of Mo_1-CuO with and without TBA.

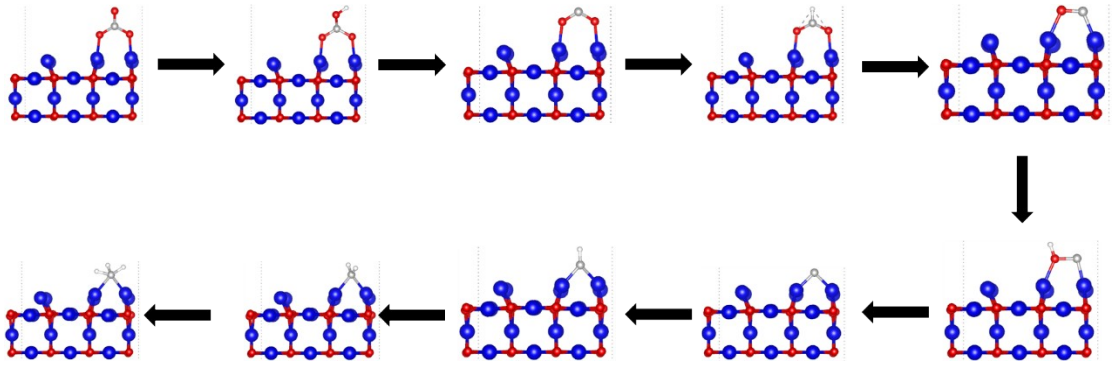

Fig. S17 Optimized adsorption configures of NO_3RR intermediates of the CuO surface.

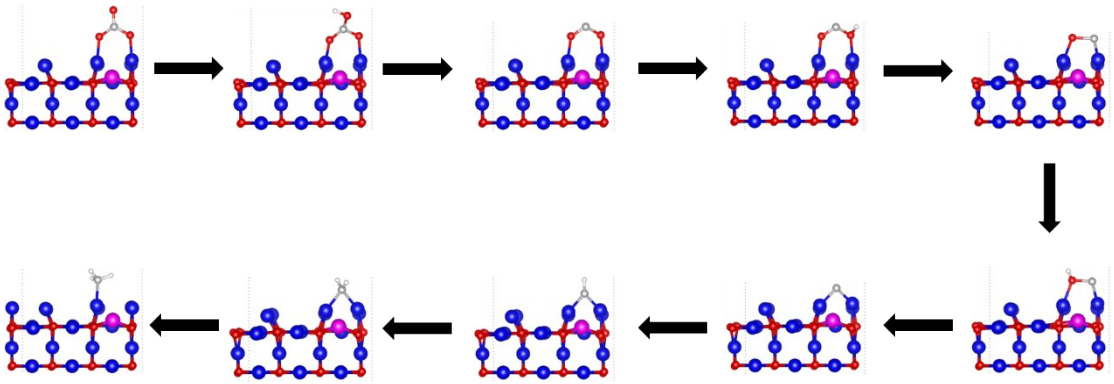

Fig. S18 Optimized adsorption configures of NO_3RR intermediates of the Mo-CuO surface.

References

1. X. Zhao, X. Zhang, Z. Xue, W. Chen, Z. Zhou and T. Mu, Fe nanodot-decorated MoS_2 nanosheets on carbon cloth: an efficient and flexible electrode for ambient ammonia synthesis, *Journal of Materials Chemistry A*, 2019, **7**, 27417-27422.
2. Z. Wang, C. Sun, X. Bai, Z. Wang, X. Yu, X. Tong, Z. Wang, H. Zhang, H. Pang, L. Zhou, W. Wu, Y. Liang, A. Khosla and Z. Zhao, Facile Synthesis of Carbon Nanobelts Decorated with Cu and Pd for Nitrate Electroreduction to Ammonia, *ACS Applied Materials & Interfaces*, 2022, **14**, 30969-30978.
3. F.-Y. Chen, Z.-Y. Wu, S. Gupta, D. J. Rivera, S. V. Lambeets, S. Pecaut, J. Y. T. Kim, P. Zhu, Y. Z. Finfrock, D. M. Meira, G. King, G. Gao, W. Xu, D. A. Cullen, H. Zhou, Y. Han, D. E. Perea, C. L. Muhich and H. Wang, Efficient conversion of low-concentration nitrate sources into ammonia on a Ru-dispersed Cu nanowire electrocatalyst, *Nat Nanotechnol*, 2022, **17**, 759-767.
4. J. Yang, H. Qi, A. Li, X. Liu, X. Yang, S. Zhang, Q. Zhao, Q. Jiang, Y. Su, L. Zhang, J.-F. Li, Z.-Q. Tian, W. Liu, A. Wang and T. Zhang, Potential-Driven Restructuring of Cu Single Atoms to Nanoparticles for Boosting the Electrochemical Reduction of Nitrate to Ammonia, *Journal of the American Chemical Society*, 2022, **144**, 12062-12071.
5. Y. Luo, K. Chen, P. Shen, X. Li, X. Li, Y. Li and K. Chu, B-doped MoS_2 for nitrate electroreduction to ammonia, *J Colloid Interf Sci*, 2023, **629**, 950-957.
6. Q. Gao, B. Yao, H. S. Pillai, W. Zang, X. Han, Y. Liu, S.-W. Yu, Z. Yan, B. Min, S. Zhang, H. Zhou, L. Ma, H. Xin, Q. He and H. Zhu, Synthesis of core/shell nanocrystals with ordered intermetallic single-atom alloy layers for nitrate electroreduction to ammonia, *Nature Synthesis*, 2023, **2**, 624-634.
7. S. Zhang, J. Wu, M. Zheng, X. Jin, Z. Shen, Z. Li, Y. Wang, Q. Wang, X. Wang, H. Wei, J. Zhang, P. Wang, S. Zhang, L. Yu, L. Dong, Q. Zhu, H. Zhang and J. Lu, Fe/Cu diatomic catalysts for electrochemical nitrate reduction to ammonia, *Nature Communications*, 2023, **14**.
8. Y. Li, Z. Lu, L. Zheng, X. Yan, J. Xie, Z. Yu, S. Zhang, F. Jiang and H. Chen, The synergistic catalysis effect on electrochemical nitrate reduction at the dual-function active sites of the heterostructure, *Energy & Environmental Science*, 2024, **17**, 4582-4593.
9. Y. Wang, F. Hao, M. Sun, M. T. Liu, J. Zhou, Y. Xiong, C. Ye, X. Wang, F. Liu, J. Wang, P. Lu, Y. Ma, J. Yin, H. C. Chen, Q. Zhang, L. Gu, H. M. Chen, B. Huang and Z. Fan, Crystal Phase Engineering of Ultrathin Alloy Nanostructures for Highly Efficient Electroreduction of Nitrate to Ammonia, *Advanced Materials*, 2024, **36**.

10. H. Liang, M. Chen, Y. Feng, G. Meng, J. Zhang, W. Liu and X. Liu, Construction of a Heterostructured Alloy–Molybdenum Nitride Catalyst for Enhanced NH_3 Production via Nitrate Electrolysis, *Inorganic Chemistry*, 2025, **64**, 1252-1257.